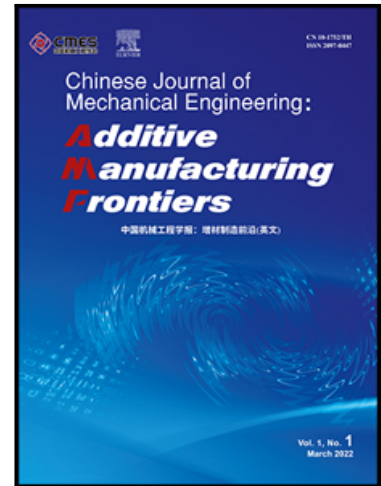# Journal Pre-proof

Laser Powder Bed Fusion-built Ti6Al4V Bone Scaffolds Composed of Sheet and Strut-based Porous Structures: Morphology, Mechanical Properties, and Biocompatibility

Shuai Ma , Qian Tang , Changbao Zhu , Fuyou Wang , Qixiang Feng , Jun Song , Rossitza Setchi , Chenglong Ma , Ran Tao

Please cite this article as: Shuai Ma , Qian Tang , Changbao Zhu , Fuyou Wang , Qixiang Feng , Jun Song , Rossitza Setchi , Chenglong Ma , Ran Tao , Laser Powder Bed Fusion-built Ti6Al4V Bone Scaffolds Composed of Sheet and Strut-based Porous Structures: Morphology, Mechanical Properties, and Biocompatibility, *Chinese Journal of Mechanical Engineering: Additive Manufacturing Frontiers* (2022), doi: https://doi.org/10.1016/j.cjmeam.2022.100051

Laser Powder Bed Fusion-built Ti6Al4V Bone Scaffolds Composed of Sheet and Strut-based Porous Structures: Morphology, Mechanical Properties, and Biocompatibility

Shuai Ma [a, b, c], Qian Tang [a, *], Changbao Zhu [d], Fuyou Wang [e], Qixiang Feng [a], Jun Song [a, c],

Rossitza Setchi [c], Chenglong Ma [f], Ran Tao [g]

a State Key Laboratory of Mechanical Transmissions, Chongqing University, Chongqing, 400044, China

b College of Mechanical Engineering, Chongqing University of Technology, Chongqing, 400054, China

c Cardiff School of Engineering, Cardiff University, Cardiff, CF24 3AA, United Kingdom

d Department of Orthopedics, General Hospital of Xinjiang Military Region, Urumqi, 830099, China

e Center for Joint Surgery, Southwest Hospital, the Third Military Medical University, Chongqing, 400038, China

f School of Mechanical Engineering, Jiangnan University, Wuxi, 214122, China

g School of Mechanical Engineering and Automation, Harbin Institute of Technology, Shenzhen, 518055, China

* Corresponding author, E-mail: tqcqu@cqu.edu.cn(Q. Tang)

Abstract

Laser powder bed fusion (L-PBF)-built triply periodic minimal surface (TPMS) structures are designed by implicit functions and are endowed with superior characteristics, such as adjustable mechanical properties and light-weight features for bone repairing; thus, they are considered as potential candidates for bone scaffolds. Unfortunately, previous studies have mainly focused on different TPMS structures. The fundamental understanding of the differences between strut and sheet-based structures remains exclusive, where both were designed by one formula. This consequently hinders their practical applications. Herein, we compared the morphology, mechanical properties, and biocompatibility of sheet and strut-based structures. In particular, the different properties and in vivo bone repair effects of the two structures are uncovered. First, the morphology characteristics demonstrate that the manufacturing errors of sheet-based structures with diverse porosities are comparable, and semi-melting powders as well as the ball phenomenon are observed; in comparison, strut-based samples exhibit cracks and thickness shrinking. Second, the mechanical properties indicate that the sheet-based structures have a greater elastic modulus, energy absorption, and better repeatability compared to strut-based structures. Furthermore, layer-by-layer fracturing and diagonal shear failure modes are observed in strut-based and sheet-based structures, respectively. The in vivo experiment demonstrates enhanced bone tissues in the strut-based scaffold. This study significantly enriches our understanding of TPMS structures and provides significant insights in the design of bone scaffolds under various bone damaging conditions.

Keywords

1. Introduction

Bone scaffolds have significantly progressed in structural design with the development of additive manufacturing (AM), which is a promising method to fabricate complex parts and various materials, consequently attracting several researchers in investigating its biomedical applications [1]. The layer-by-layer process allows manufacturing scaffolds that can mimic the shape of damaged bone [2]. Laser powder bed fusion (L-PBF) allows the manufacture of bone scaffolds using various metallic powders, such as iron-manganese [3], Ti6Al4V [4, 5], 316L stainless steel [6, 7], and NiTi [8]. Therefore, porous metallic structures have recently gained significant attention for the bone scaffold design because they can provide a connected internal space for bone cell growth and repair [9].

There are various porous structural categories including honeycomb [10] and centered cubic structures [11]. However, triply periodic minimal surface (TPMS) structures are considered as appropriate candidates for bone scaffolds, heat dissipation, and shock absorption owing to their lightweight and adjustable mechanical properties [12-14]. TPMS structures have a large surface area, which is beneficial for bone cells to attach to; the surface is smooth and continues with a zero mean curvature, which is similar to human bone [15]. Furthermore, TPMS structures are ideal filling structures because they have periodic repeatability. The shapes of TPMS structures are controlled by their primitive functions, and designing different shapes is enabled by changing the shape parameter. Generally, the different shapes obtained from the same primitive function can be divided into the following two categories: strut-based and sheet-based structures [16-18]. Furthermore, to achieve a functional design, graded structures can be modelled by changing the shape parameter along one direction [19]. These design methods can expand the application of TPMS structures; therefore, TPMS structures have gained attention for further research. Schwarz Primitive (Schwarz-P) is a classic structure of TPMS, which consists of a smooth and continuous surface and an average curvature of zero. Jung et al. indicated that Schwarz-P has the best permeability among six TPMS structures [20]; permeability is regarded as an important influence factor in the early stage of bone repair [21]. Bobbert et al. fabricated four types of TPMS structures, including Schwarz-P, and compared the mechanical properties of TPMS structures with human bone. The results demonstrated that the elastic modulus of the TPMS structures was in the range of trabecular bones, and the yield stress was higher [22]. Heran et al. studied the relationship between the designed porosity, thickness, and elastic modulus of Schwarz-P structures [23]. Yu et al. proposed a graded design method to improve the energy absorption ability of Schwarz-P structures [24]. Therefore, Schwarz-P was chosen as the classic representative of TPMS structures in this study.

Morphological characteristics related to the manufacturing quality include the manufactured error and roughness, both of which can affect the mechanical properties; bone repair can be affected by rough and smooth surfaces [25]. Choy et al. indicated that the orientation of structures can affect powder adhesion, which will influence the differences between the designed and measured thickness [26]. Xu et al. manufactured a series of thin-walled structures with a thickness ranging from 0.05 mm to 1 mm. Their results demonstrated that all the measured thicknesses were greater than the designed value, and the error was greater for the low-designed structure [27]. Ataee et al. studied the roughness (Ra) of strut-based gyroid structures ranging from 3.2 μm to 5 μm [28]; however, the roughness of the top and side surfaces were not studied individually.

The mechanical properties of human bone cover a large range. Rho et al. indicated that the Young's modulus of trabecular bone is approximately 0.76 to 20 GPa [29]. To avoid stress-shielding [30], the mechanical properties of L-PBF-built scaffolds should mimic the damaged bone. The mechanical properties of TPMS structures were studied herein owing to their adjustable and wide-ranging elastic modulus. Al-Ketan et al. studied the mechanical properties of various strut-, skeletal-, and sheet-based maraging steel structures; the results indicate that sheet-TPMS-based structures have better mechanical properties [18]. Li et al. researched the energy absorption of stereolithography-built strut-based and sheet-based gyroid structures, demonstrating that the sheet-based structures have a greater elastic modulus and yield strength and are more suitable for energy absorption [31]. Soro et al. designed three types of Schwarz-P strut-based scaffolds with a 25% to 64% porosity; the Young's modulus ranged from 22.3 GPa to 58 GPa [32]. Although the aforementioned studies investigated the mechanical properties of TPMS structures, most of the designed porosities and elastic moduli were too high for bone repairing. Furthermore, most of the studies failed to distinguish and analyze strut- and sheet-based structures. These two structures are modelled by the same primitive function but have different geometric shapes; as a result, the morphology, mechanical properties, and bone repair effect of these structures under the same porosity are not sufficiently understood.

To address this challenge and expand the design options and applications of the TPMS structures for different bone repairing requirements, sheet-based and strut-based Schwarz-P Ti6Al4V scaffolds were designed and fabricated in this study with porosities ranging from 60% to 85%. The manufactured porosity, thickness, relative density, and roughness were compared to investigate the differences in morphology. To thoroughly understand the differences in the mechanical properties, the elastic modulus, yield strength, energy absorption, and failure modes were systematically studied for both types of scaffolds. The novelty of this study is its revelation of the various mechanical behaviors and in vivo bone repair effects of these two structures. This study significantly enhances the understanding of TPMS structures, provides a more reliable basis for the selection of a TPMS structure type and design parameters, and expands the design concept of TPMS structures in bone scaffolds and other related fields.

2. Research Method

2.1 . Powder characteristics

Ti6Al4V powders (Ti Bal., Al: 5.5%–6.75%, V: 3.5%–4.5%, Cmax: 0.08%, et al.) were provided by TLS Technik Ltd. The micromorphology of the Ti6Al4V powders was observed using scanning electron microscopy (SEM) (FEI Nova 400 FEG-SEM, 300 × 20 kV). As shown in Fig. 1(a), most powders had a spherical shape, whereas a few powders had an irregular shape. Image J software was used to calculate the percent distribution of the powders, as shown in Fig. 1(b). D10, D50, and D90 indicate the proportion of powders with diameters below them as 10%, 50%, and 90%, respectively. The mean diameter of the Ti6Al4V powders was 35.25 μm.
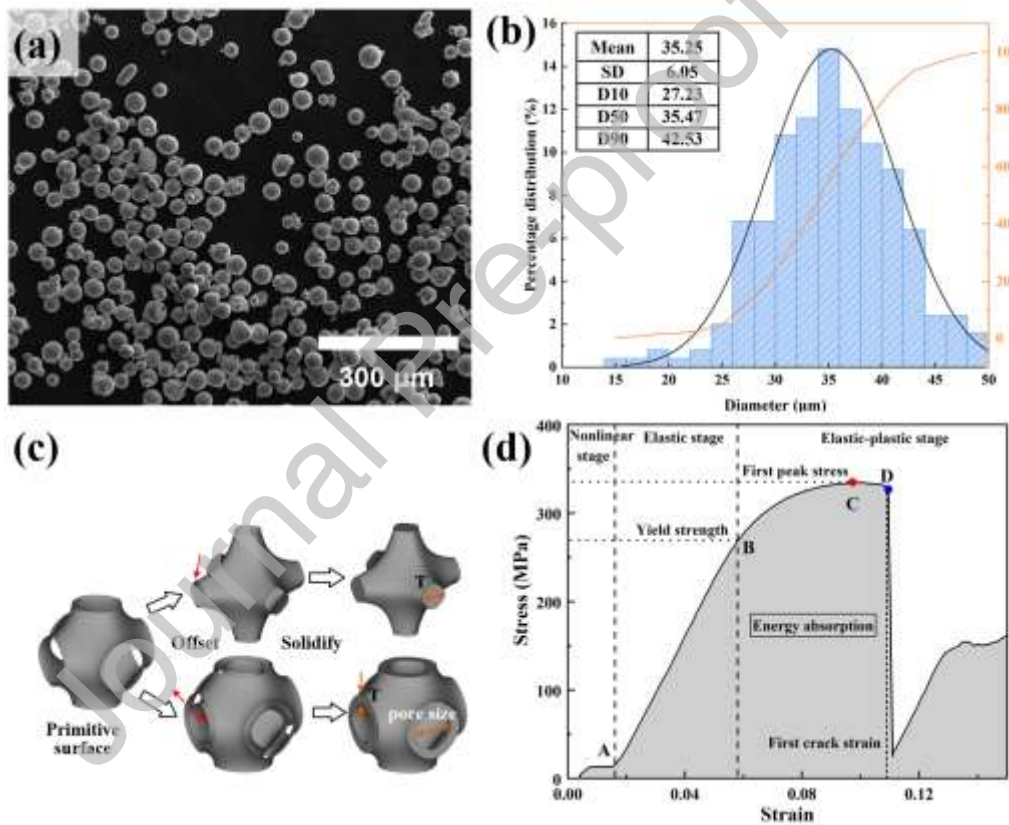
Fig. 1. (a) SEM image of the Ti6Al4V powders; (b) Percentage distribution and cumulative frequency of the powders; (c) Modelling process of sheet-based (bottom) and strut-based (top) Schwarz-P structure units; (d) Stress-strain diagram of the compressive experiments.

2.2 Design and manufacturing

Sheet-based and strut-based Schwarz-P structures are modelled from the primitive surface and offset surface as described by Eqs. (1), and (2) and (3), respectively:

$$\varphi(x, y, z) = \cos x + \cos y + \cos z = 0 \ , \tag{1}$$

$$\varphi_{\text{offset}}(x, y, z) = \varphi\left(x - \frac{1}{tR} \times \frac{d\varphi}{dx}, y - \frac{1}{tR} \times \frac{d\varphi}{dy}, z - \frac{1}{tR} \times \frac{d\varphi}{dz}\right) = 0 \ , \tag{2}$$

$$R(x, y, z) = \sqrt{\left(\frac{d\varphi}{dx}\right)^2 + \left(\frac{d\varphi}{dy}\right)^2 + \left(\frac{d\varphi}{dz}\right)^2} \ , \tag{3}$$

where t controls the offset distance. As shown in Fig. 1(c), to create a sheet-based structure, the surface can be offset along with two normal directions with the same distance, solidifying the volume between these two offset-surfaces; T is the thickness. To create a strut-based structure, the volume in $\varphi_{\text{offset}}(x, y, z) < 0$ can be solidified.

Five types of units with porosities ranging from 60% to 85% were designed for both sheet-based and strut-based structures(Fig. 2). To obtain the same porosity for the sheet-based and strut-based structures, the unit lengths of the strut-based structures were adjusted as shown in Table 1. The samples for the compression test and in-vivo experiments were then built by arraying the unit structure, comprising 20 mm length cubes, and cylinders with a 6 mm diameter and 6 mm height, respectively.
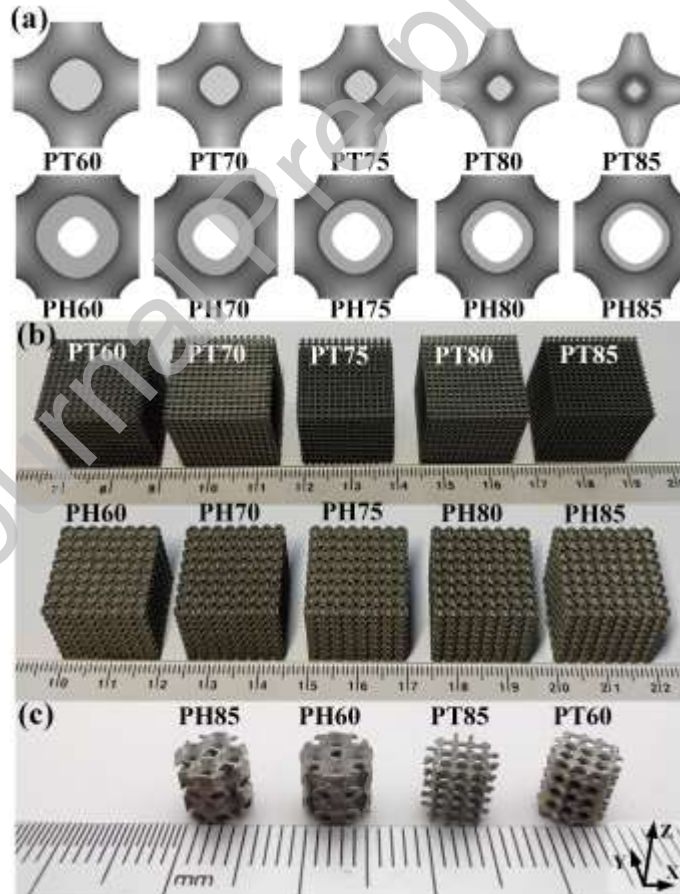
Fig. 2. (a) Designed strut-based and sheet-based Schwarz-P units; (b) As-built samples for the compression tests; (c) Samples for the in-vivo experiments.

Table 1. Characteristics of the designed porous unit

Unit name	Porosity (%)	Thickness (mm)	Pore size (mm)	Unit length (mm)	Area (mm^2)
PH60	60	0.44	0.81	2.5	20,276
PH70	70	0.32	0.93	2.5	19,364
PH75	75	0.27	0.98	2.5	18,733
PH80	80	0.22	1.03	2.5	18,361
PH85	85	0.16	1.09	2.5	17,801
PT60	60	0.57	0.81	1.38	17,344
PT70	70	0.44	0.93	1.37	15,539
PT75	75	0.36	0.98	1.34	13,877
PT80	80	0.28	1.03	1.30	13,031
PT85	85	0.17	1.09	1.26	11,348

The parts were fabricated using SLM 500 (Solutions, Germany) with a 240 W laser power, 0.12 mm scan interval, 1100 mm/s scan speed, 0.075 mm spot diameter, and 0.03 mm layer thickness. The building direction was named the *z*-axis. All parts were removed from the building platform by wire electrode cutting, cleaned using an ultrasonic bath, and sandblasted to remove the remaining powders.

2.3 Morphology and mechanical properties experiments

An optical microscope (VHX-1000 digital microscope) was used to measure the thickness of each type of structure. Each sample was measured approximately 25 times, and the mean value was calculated. The error of thickness was calculated using Eq. (4). Furthermore, the morphology of the surface was also observed by optical microscopy.

$$E_{\text{thickness}} = T_{\text{designed}} - T_{\text{measured}}, \tag{4}$$

where $E_{\text{thickness}}$, T_{designed}, T_{measured} represent the error of thickness, and designed and measured thicknesses of the sample, respectively. An electronic balance (HZY-A120, USA, 0.001 g) was used to measure the mass of each sample in air m_a and water m_w (20 ℃). The relative density R_d was calculated using the Archimedes method as follows:

$$R_d = \frac{\rho_{\text{water}}}{\rho_{\text{Ti6Al4V}}} \times \frac{m_a}{m_a - m_w} \times 100\%, \tag{5}$$

where ρ_{water} and ρ_{Ti6Al4V} represent the density of water and the Ti6Al4V solid material in this study, which was 0.998 g/cm^3 and 4.51 g/cm^3, respectively. The as-built porosity and error of porosity can also be studied via Eqs. (6) and (7), respectively:

$$P_{\text{as-built}} = \left(1 - \frac{m_a}{m_{\text{solid}}}\right) \times 100\%, \tag{6}$$

$$E_{\text{porosity}} = P_{\text{designed}} - P_{\text{as-built}}, \tag{7}$$

where $P_{\text{as-built}}$, m_{solid}, E_{porosity}, and P_{designed} represent the as-built porosity, mass of solid cube, error of porosity, and designed porosity, respectively. Considering the complex structures of the porous samples, the non-contact 3D surface profiler (Sensofar Co., Spain) was used to measure the roughness (Ra) of both the top and side surfaces of each sample. Two random spots (1700 μm× 1418 μm) were chosen for each surface, and at least three random lines were chosen to be measured in each spot. Scanning electron microscopy (SEM) (Zeiss 1540XB) was used to observe the fracture morphology of the compressed samples and the interior surface, with a 10 kV parameter.

2.4 Compressive experiments

To calculate the mechanical properties and energy absorption, universal testing machines (Avery Denison 600 kN, Avery-Denison Limited, UK; MTS793, MTS Co., USA; WAW-600, SUNS, China) were used to process the compressive experiments. The upper crosshead moved along the *z*-axis with a 2 mm/s rate and loaded on the top surface of the tested sample. A strain of at least 0.5 was tested for all the samples, and the compression process was recorded by a 60 f/s camera. The elastic modulus E_p and yield strength σ_p of the porous samples can be estimated from the stress-strain diagram. As shown in Fig. 1(d), the compressive process consists of the following three stages: nonlinear, elastic, and elastic-plastic. The slope of the *AB* curve in the elastic stage is defined as the elastic modulus. The stress of the first peak point *C* and the strain of the first stress-drop point *D* are defined as the first peak stress (σ_f) and first crack strain, respectively.

The energy absorption properties of the porous structures were calculated using Eqs. (8) and (9) as follows:

$$W = \int_0^\varepsilon \sigma(\varepsilon)\mathrm{d}\varepsilon \ , \tag{8}$$

$$W_E = \frac{\int_0^\varepsilon \sigma(\varepsilon)\mathrm{d}\varepsilon}{\sigma(\varepsilon)}, \tag{9}$$

where W (MJ/m^3) is the energy absorption per unit volume of the porous structure, which is the area under the stress-strain curve shown in Fig. 1(d). W_E is the efficiency of the energy absorption; ε and σ indicate the strain and stress of the compressive stress-strain curve, respectively.

2.5 In vivo experiment

The in vivo experiment plan was approved by the Laboratory Animal Welfare and Ethics Committee of the Third Military Medical University. To reduce the number of animals used, four scaffolds were implanted:

PH60, PH85, PT60, and PT85. The implanting process is shown in Fig. 3(a). The scaffolds were implanted into the holes, which were drilled 6 to 7 mm deep by a 6.5 mm diameter drill and located at the femur or tibia; the bone debris was used to fill the gap between the scaffold and host bone. Two healthy Guizhou miniature pigs were operated on and raised for 4 weeks in this study; the pigs were then sacrificed to obtain the bone-scaffold segments. To analyze the growth of bone tissue in the scaffolds, the bone-scaffold segments were fixed with formalin for 48 h, modified to 10 mm × 10 mm × 10 mm cubes through a hard tissue microtome (EXAKT300CP, Germany), and then fixed for another 24 h. All segments were dehydrated by 50%, 75%, 95% and 100% graded ethanol, and each step was processed for 24 h. All bone-scaffold segments were then immersed in a solution consisting of anhydrous ethanol and resin (Technovit 7200, ratio 1:1) for 2 days, then soaked in the resin for 5 days and embedded through an embedding machine (EXAKT520, Germany). To observe the bone repaired effect of different areas of the scaffolds (Fig. 3(b)), 6 slices were cut around the horizontal direction using a hard tissue microtome. These slices were located at the top, middle, and bottom of the scaffolds and had a thickness of 200 μm; these slices were grinded to 50 μm using a grinding machine (BROTLAB, France) with 800#, 1200#, 2000# and 4000# sandpapers. All slices were stained with Masson and Sirius red; the effect of the scaffolds on bone repair was then observed and recorded by an optical microscope (szm-7045, Omu Micro Technology, China).
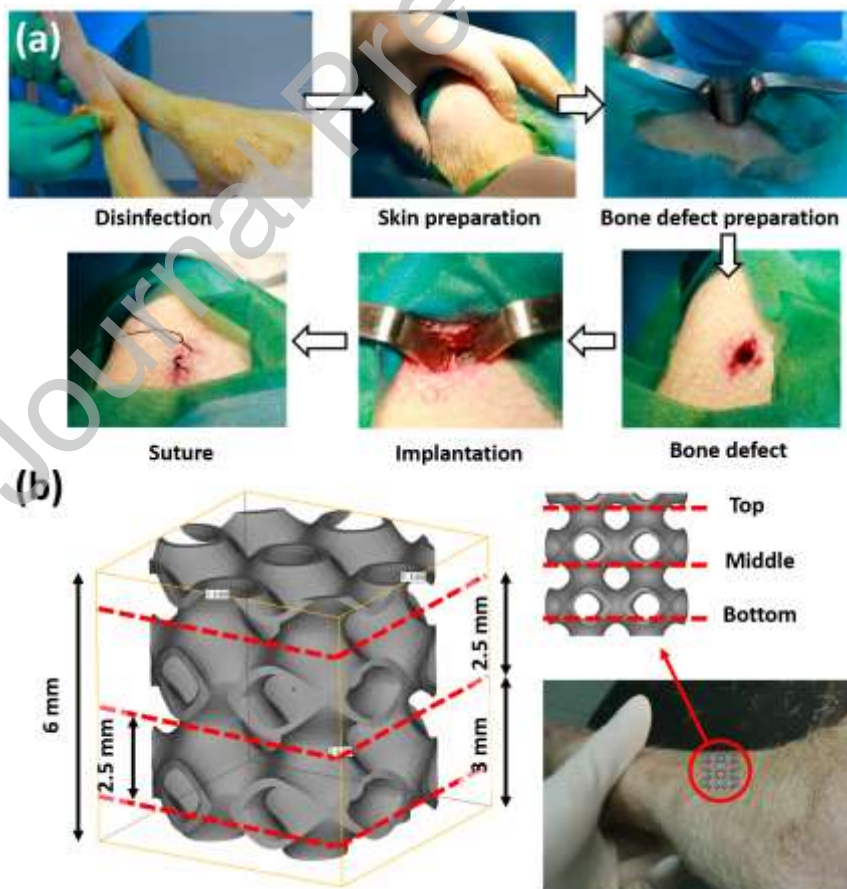

Fig. 3. (a) Process of implantation; (b) Cutting positions of the scaffold slices.

3. Results and Discussion

3.1 Morphology characteristics

3.1.1 Manufacturing errors and defects

The measured and designed thicknesses are shown in Fig. 4(a). All measured thicknesses were lower than the designed values, which was also observed in the study by Choy et al. [26], except for the 85% porosity strut-based PT85 sample. The results demonstrate that the curve of the thickness error has a platforming trend for the structures with 60% to 75% porosity; however, overall, the error of thickness decreased with the increase in porosity. For porosity, most of the as-built samples measured lower than the designed values; the same results were found in another study [33]. The error of porosity generally increased with an increase in the designed porosity, except for PT85. This may be caused by the remaining semi-melting powders and the balling phenomenon on the surfaces, as shown in Fig. 4(c) and (d). These remaining powders increased the mass of the structures, decreased the porosity, and had a greater effect on the samples that were designed with a high porosity. This is because the increased mass caused by the remaining powders obtains a larger proportion of the mass of the samples with a high porosity [21]. Fig. 4(c), (d) also demonstrates that the sheet-based structure has more remaining powders than the strut-based sample, thus the trend of the porosity error of the sheet-based structure is more stable. These adhesive powders, which are not hanged on the side surface, can also improve the mechanical properties of the samples.
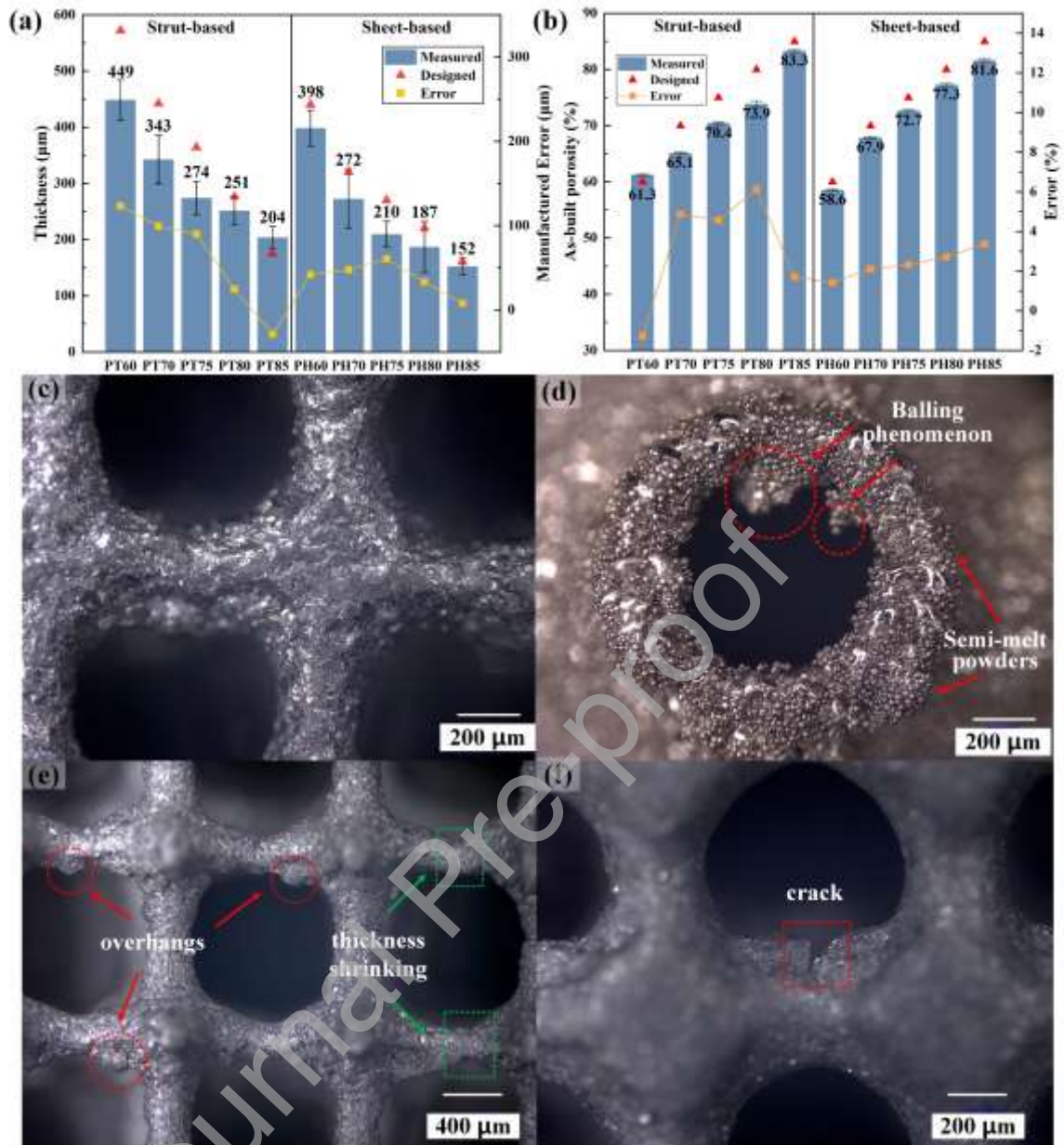
Fig. 4. (a) Measured and designed thickness and manufactured error of the specimens; (b) Measured porosity and manufactured error (values in the figure are measured values); (c) Strut-based; (d) Sheet-based Schwarz-P scaffold with 80% porosity; Manufacturing defects of (e) PT85 and (f) PT70.

Note, the results of the thickness and porosity appear inconsistent: the as-built thickness was lower than the designed thickness, which indicates that the as-built porosity should be higher than the design value; however, the results present the opposite. This phenomenon can be explained as follows:

(1) The thickness was measured on the outermost layer of the samples, and tended to reflect the local characteristics; however, the porosity tends to reflect the global feature.

(2) The outermost layer was the farthest hanging part of the porous unit, where it is most likely for manufactured defects to occur [34, 35]. As shown in Fig. 4(e), the thickness shrinks at the connection boundary of the units; cracking was observed at PT70, as shown in Fig. 4(f).

(3) The remaining powders and the balling phenomenon on the surface reduce the as-built porosity. Explanation (2) also indicates why the thickness errors decline with an increasing porosity, which is because the designed lengths of the unit cubes decline with an increasing porosity, indicating that the hanging distance also declines. Another reason is that the thickness of the higher porosity samples is near the minimum limit of the manufactured thickness in the L-PBF process [27].

As shown in Fig. 5, for strut-based scaffolds, the relative density of the 60% porosity sample is near that of the block at approximately 97%, and the relative density declines as the porosity increases. This indicates that the high-designed porosity samples (thin samples) easily have a lower relative density. For sheet-based structures, the 60% porosity samples also presented the largest relative density. The relative density of sheet-based structures is generally slightly lower than that of strut-based structures. This is also because the designed thickness of the strut-based structures is larger. However, the bubbles should not be ignored, which make the results of relative density smaller; these bubbles form on the semi-melt powders on the surface of the sheet-based samples in the experiment process.
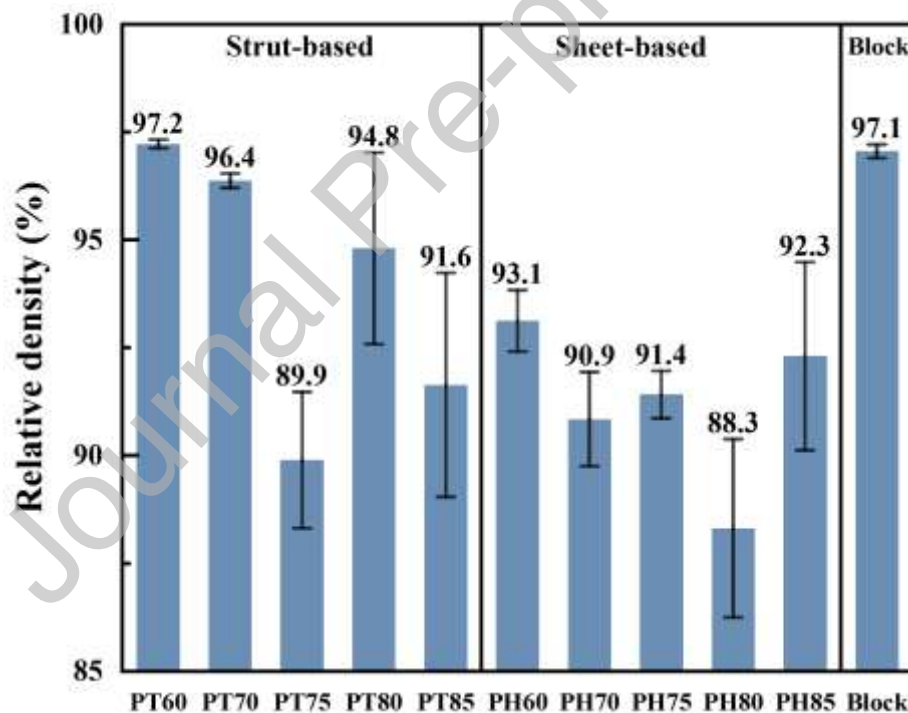

Fig. 5. Relative density of strut-based and sheet-based Schwarz-P scaffolds and the Ti6Al4V solid block.

3.1.2 Roughness of samples

Fig. 6(a) demonstrates the roughness of two types of Schwarz-P samples. The roughness results are similar for samples with the same type of structure, ranging between 0.29 μm to 0.94 μm. However, the roughness of sheet-based samples is evidently larger than that of strut-based structures at approximately 3 μm. Based on Table 1, the area of the sheet-based sample is larger than the strut-based structure with the same porosity because the sheet-based samples have a greater chance of remaining semi-melt powders on the surface, which

enhances the roughness, as shown in Fig. 4(d). In the strut-based structure group, the side surfaces are rougher than the top surfaces (except PT60, which is close), and the maximum difference can reach approximately 3 times that of the top surface. This phenomenon is caused by the manufacturing feature of the L-PBF process; the same results were observed in other studies [36, 37]. However, this trend is insignificant for sheet-based samples: the side surfaces of PH75 and PH80 are smoother than the top surface. This can be explained by the geometric feature of outer surfaces, which is shown in Fig. 6(b); in sheet-based samples, the proportion of the length of the vertical part (L_v) to the unit length is small. This indicates that the roughness of the side surface is less affected by the vertical part, which indicates that the rule of "the side surface being rougher than top surface" is not suitable for sheet-based structures.
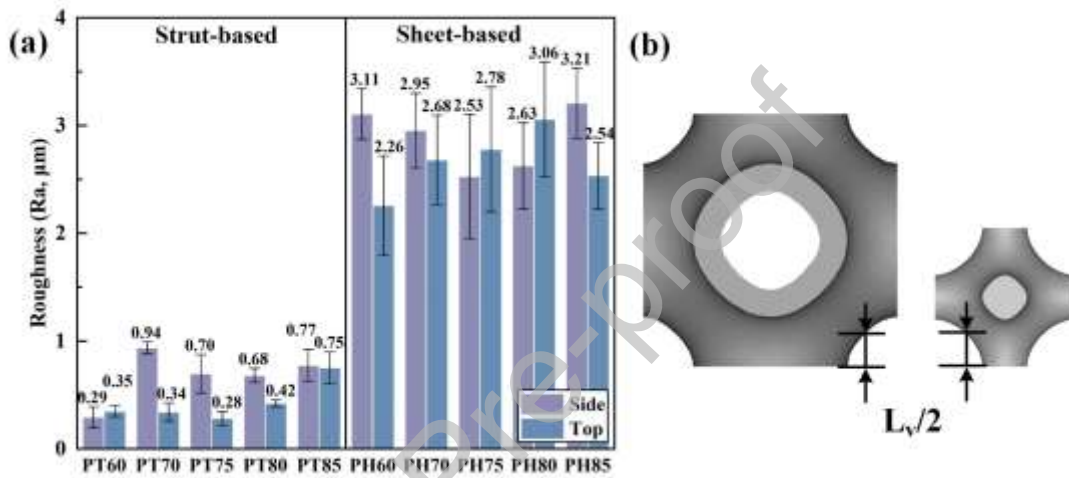
Fig. 6. (a) Roughness of side and top surfaces of strut-based and sheet-based Schwarz-P structures; (b) Length of the vertical part for PT70 and PH70.

The morphology characteristics of two types of Schwarz-P structures at different porosities are compared in this section. The manufactured errors of the thickness and porosity of sheet-based structures are more stable; the strut-based structures have a higher relative density, and the surfaces of sheet-based structures are rougher owing to more remaining powders.

3.2 Mechanical properties and energy absorption

3.2.1 Mechanical properties and failure modes

The mechanical properties were calculated using the compression tests; the results are shown in Table 2. The elastic moduli of strut-based samples ranged from 1287 MPa to 3962 MPa, while those of the sheet-based samples ranged from 1917 MPa to 6307 MPa. The elastic modulus of strut- and sheet-based samples were similar for the samples with 75% and 80% porosity. For the samples with other porosities, the elastic modulus of sheet-based structures was greater, which is in agreement with Al-Ketan et al. [18]. Note, the E value of PH60 was approximately 2300 MPa greater than PT60, which was the maximum difference. The yield

strength is defined as the stress of the last spot B of the elastic stage shown in Fig. 1(d): the σ of sheet-based structures is greater than strut-based structures for each porosity, ranging from 88 MPa to 272 MPa and 55 MPa to 219 MPa, respectively. The first peak stress is the maximum stress the sample can bear before the first stress decrease; thus, representing the maximum bear capacity. The results indicate that sheet-based structures can bear a higher stress before the first failure.

Table 2. Mechanical properties of Schwarz-P structures

		Elastic modulus E (MPa)	Yield strength σ(MPa)	First peak stress σ_f(MPa)	Energy absorption (MJ / m^3)
Strut-based	PT60	3962 ± 305	219 ± 8	285 ± 23	84.5 ± 10.9
	PT70	3509 ± 304	148 ± 5	186 ± 17	68.6 ± 8.9
	PT75	3146 ± 572	123 ± 1	157 ± 11	42.2 ± 2.0
	PT80	2440 ± 137	88 ± 9	96 ± 12	21.6 ± 1.23
	PT85	1287 ± 152	55 ± 4	58 ± 7	14.1 ± 0.7
Sheet-based	PH60	6307 ± 397	272 ± 7	333 ± 2	119.0 ± 1.6
	PH70	4978 ± 150	189 ± 15	224 ± 3	75.0 ± 1.1
	PH75	3259 ± 126	141 ± 4	174 ± 3	59.3 ± 3.2
	PH80	2433 ± 192	114 ± 4	136 ± 3	45.0 ± 1.6
	PH85	1917 ± 290	88 ± 3	98 ± 2	32.6 ± 0.4

Fig. 7(a) and (b) demonstrate the stress-strain diagram of the strut-based and sheet-based samples, respectively. For strut-based samples, the strain of the first crack point increased with a decrease in porosity; the first crack strain is 0.12 for PT60, and the value is 0.065 for PT85. Sheet-based structures present a similar trend; however, with a small difference between the first crack strain of PH60 and PH85. Overall, the first crack strain of sheet-based structures is concentrated at approximately 0.1. This suggests that sheet-based structures are more stable and can withstand a greater strain before the first crack. Note, there are no apparent elastic-plastic stages for PT80 and PT85; their yield strength is close to the first peak stress.
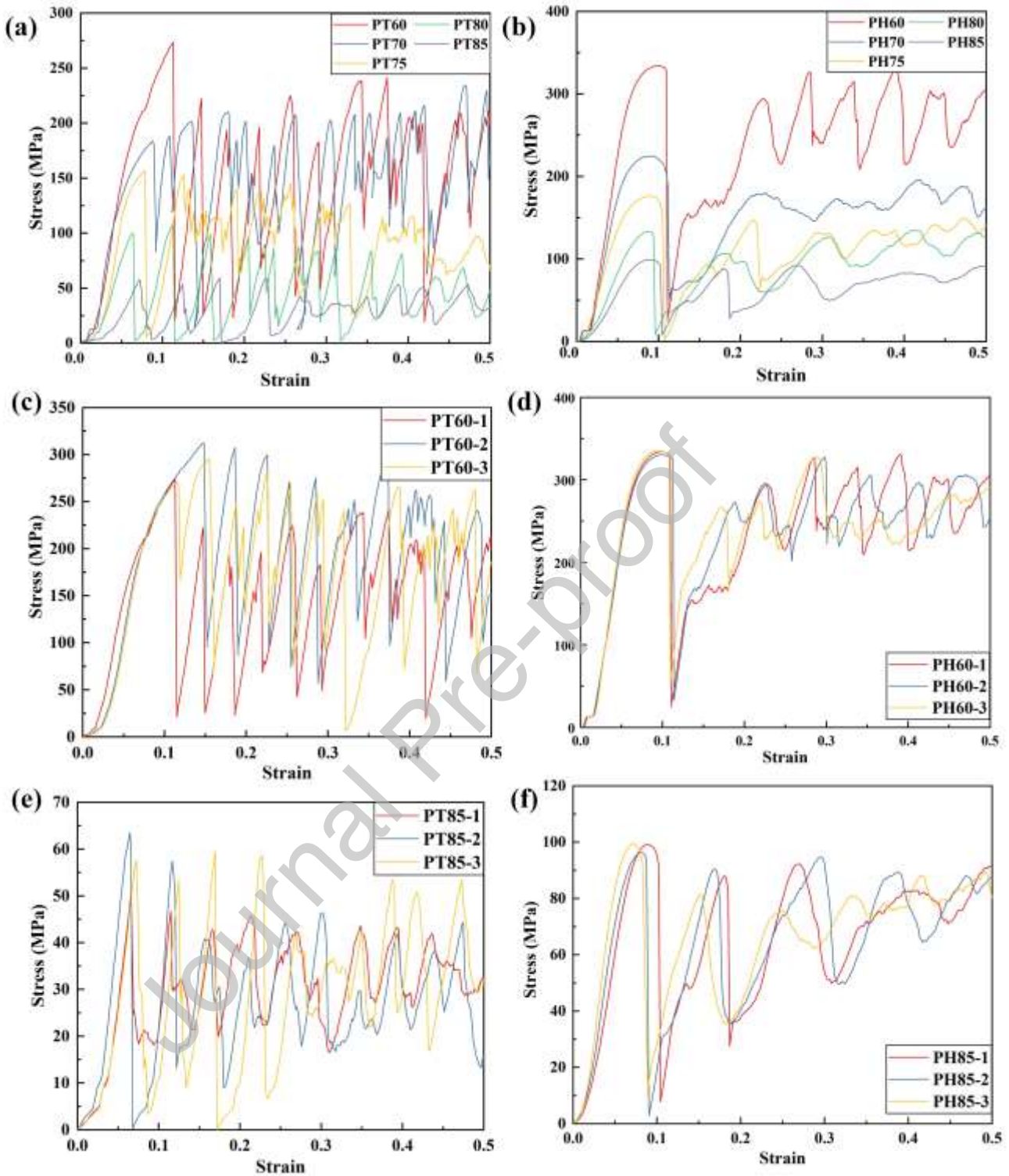
Fig. 7. Stress-strain diagram of all structures: (a) Strut-based structures; (b) Sheet-based structures; (c) Strut-based samples with 60% porosity; (d) Sheet-based samples with 60% porosity; (e) Strut-based samples with 85% porosity; (f) Sheet-based samples with 85% porosity.

The curves of the sheet-based structures rise and fall repeatedly but tend to plateau, and the amplitude decreases gradually after the first stress-drop; the curves of the strut-based samples fluctuate with a large

amplitude after the first crack point. These results are caused by the different failure modes shown in Fig. **8**. The following two different failure modes were observed in the compression tests: layer-by-layer fracturing and diagonal shear. All the strut-based structures failed in the layer-by-layer fracturing mode; the compressive process of PT70 is shown in Fig. 8(a) to represent this failure mode. The first fracture occurred at a strain of 0.117, as shown in the red box; the second collapse occurred in the fifth layer at a strain of 0.133. The stress dramatically decreases when an entire layer collapses. Therefore, this type of failure mode causes the stress-strain curves of strut-based structures to violently fluctuate several times. A 45° diagonal shear was observed in the compressive process of all sheet-based structures. As shown in Fig. 8(b), the units located at the 45° diagonal shear collapsed at a strain of 0.113; the diagonal shear is indicated by the red box. Destruction of the entire layer was not observed in the compressive process; only a portion of the units were destroyed in each layer. This failure did not cause the stress-strain curves to violently fluctuate   following the 45° diagonal shear.
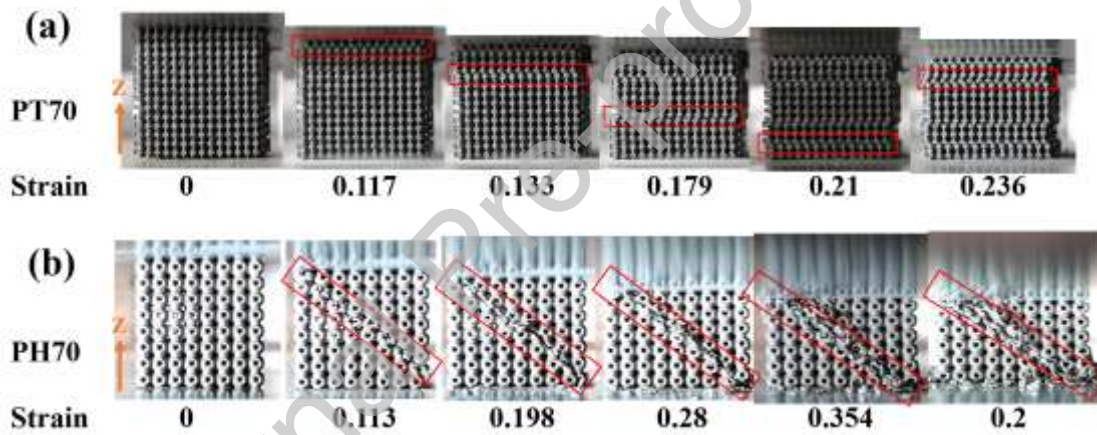

Fig. 8. Failure modes of (a) PT70 and (b) PH70.

Fig. 7(c) to (f) demonstrate the stress-strain curves of these two types of structures at porosities of 60% and 85%. The PH60 and PH85 curves present good consistency prior to the first crack, while the PT60 and PT85 curves do not. This is because the strut-based samples have certain manufacturing defects at the junction boundary of the unit, such as shrinkage and cracks. These defects affect the mechanical behavior of the strut-based samples and reduce the consistency of repeated experiments.

To investigate the fracture mode and microstructures of the fractured surfaces for each type of scaffold, the samples with 70% porosity were captured via SEM under various magnifications, as shown in Fig. 9. Fig. 9(a) to (c) demonstrates that the fracture surface was rough with deep dimples, which indicates that the fracture mode of the sheet-based scaffold with 70% porosity was ductile fracture. The horizontal fracture surface of the strut-based scaffold is shown in Fig. 9(e) and (f), where dimples were also found; however, they were not as deep as those of the sheet-based scaffold. Furthermore, no dimples were observed on the vertical fracture

surface and it was smoother than the horizontal surface; a few fractured fragments were left on the surface. For the strut-based scaffold with 70% porosity, the fracture mode of the horizontal strut was ductile fracture, whereas it was brittle fracture for the vertical strut. As shown in Fig. 8(a) andFig. **7**(a), the vertical struts lost stability and were laterally displaced upon compression, indicating that they were subject to shear forces and instantly fractured, which is consistent with the stress-strain curve.
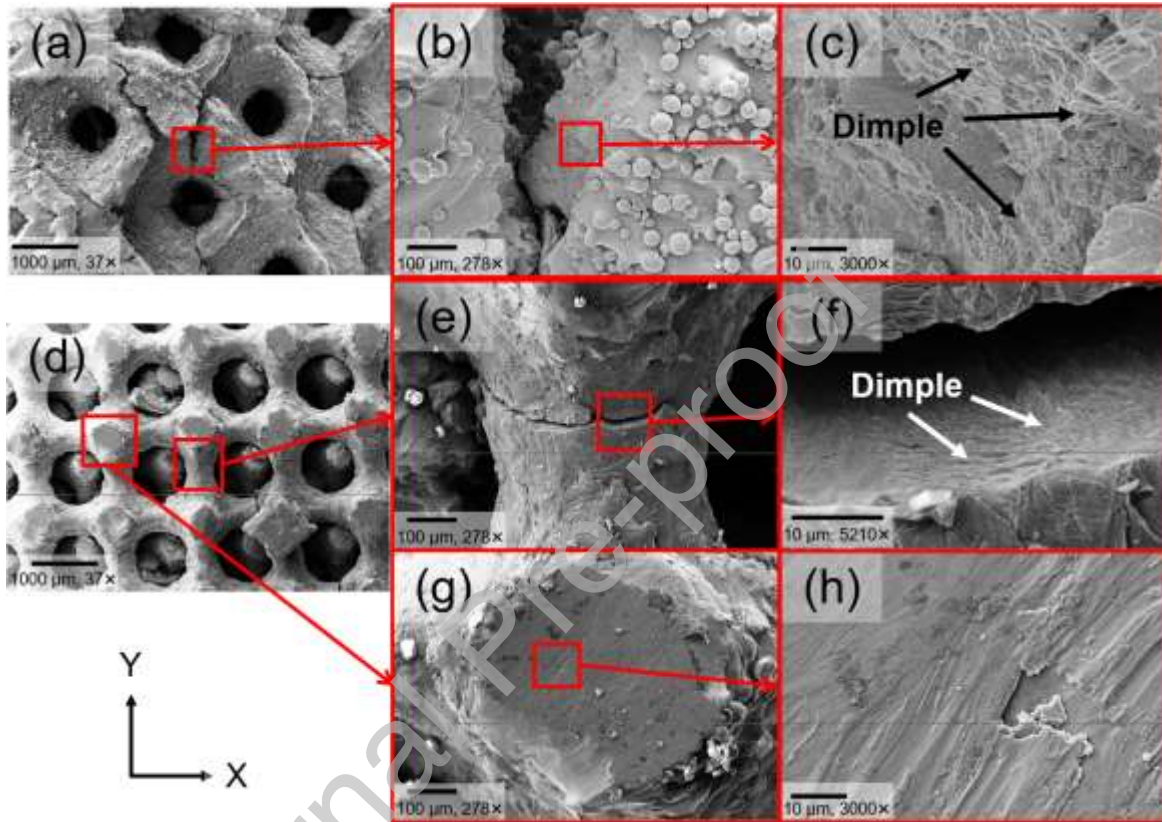

Fig. 9. SEM images of the fracture surfaces of the strut- and sheet-based samples with 70% porosity: (a-c) Sheet-based scaffold; (d) Strut-based scaffold; (e, f) Horizontal fracture surface. (g, h) Vertical fracture surface.

3.2.2 Energy absorption

The energy absorption can reflect the ability of the sample to resist deformation. Fig. 10(a) and (b) demonstrates the relationship between the energy absorption and strain and compares the energy absorption of strut-based and sheet-based structures at a strain of 0.5. The energy absorption of strut and sheet-based structures ranges between 14 MJ/m^3 to 84 MJ/m^3 and 33 MJ/m^3 to 119 MJ/m^3, respectively; hence, sheet-based samples absorb more energy under each porosity. Furthermore sheet-based structures absorb more energy at any strain, except at certain parts of the curve for the samples with 70% porosity. To estimate the efficiency and stability of the energy absorption, the relationship of the energy absorption efficiency with strain is shown in Fig. 10(c) and (d), where the full and dotted lines indicate strut-based and sheet-based structures, respectively. Here, all of the efficiency curves increased as the strain increased; however, the two

types of structures presented different trends. The curves of the sheet-based structures reach a high value at the first crack strain and then remain stable, whereas the curves of the strut-based structures violently fluctuate several times; similar to the stress-strain curves, this was caused by the layer-by-layer failure mode. In addition, there is no relationship between the efficiency of energy absorption and the porosity of the samples; the average efficiency of the samples with varying porosities is analogous.

The results for the mechanical properties indicate that sheet-based structures have more stable and stronger mechanical properties; they can also be used in applications such as buffer structures to absorb energy. Strut-based structures can also be used in safety stress protection situations.
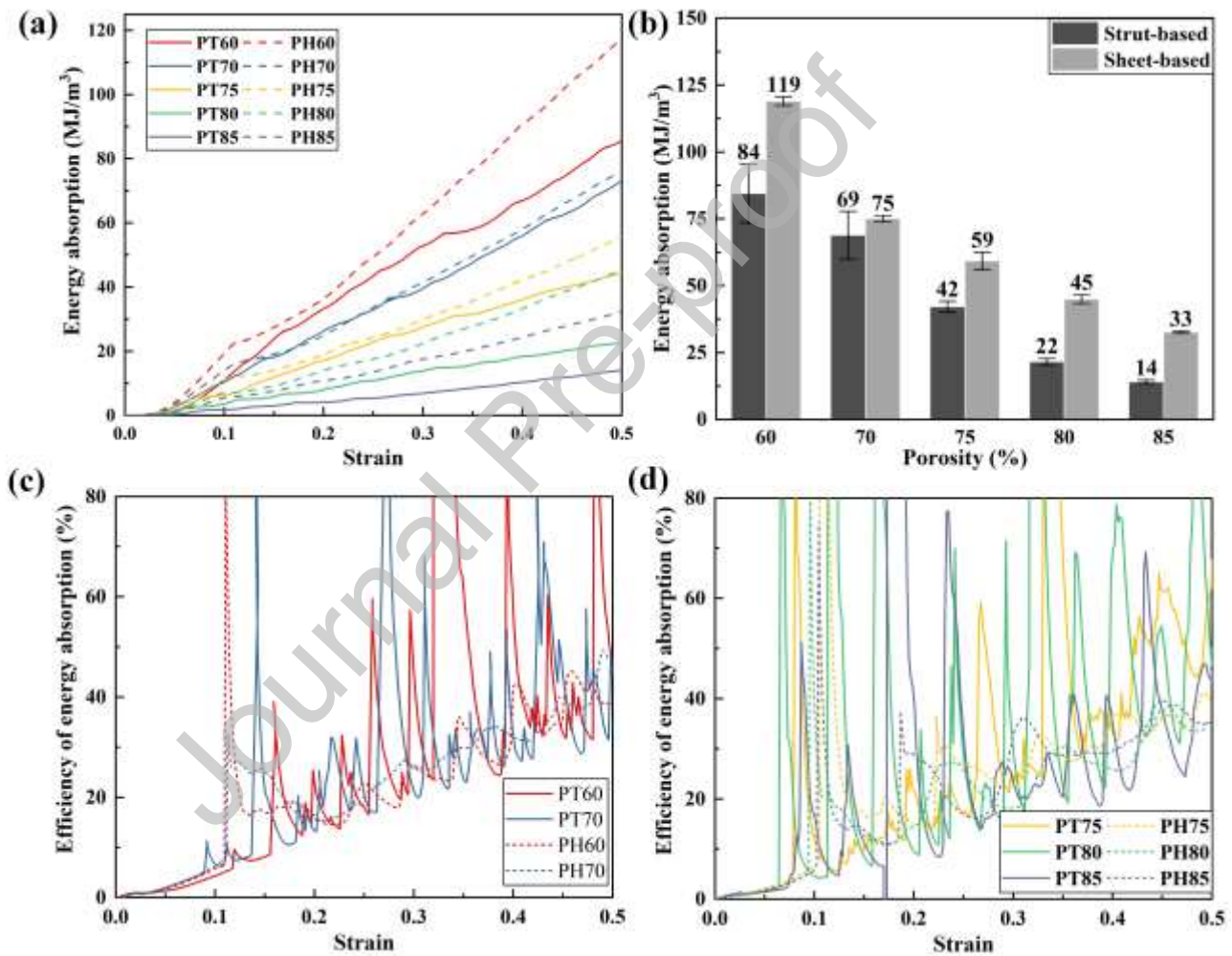

Fig. 10. (a) Energy absorption—strain diagram; (b) Energy-porosity diagram; Energy absorption efficiency of samples with (c) 60% and 70% porosity, and (d) 75%, 80%, and 85% porosity.

3.3 In vivo experiment results

3.3.1 Masson staining

Masson staining reflects the growth of soft tissue, while Sirius red staining focuses on bone tissue. As

shown in Fig. 11, for Masson staining, the red, purple, and blue/green parts indicate mature collagen type I, muscle fiber, and immature collagen type II, respectively. They can reflect the situation of bone regeneration; blue/green indicates newly grown soft tissue. The results here indicate that all the scaffolds provide a suitable microenvironment for the growth of bone cells; the soft tissue grew in and surrounded each scaffold, which can enhance the binding strength between the bone scaffold and bone tissue. For the strut-based scaffolds, the top and middle slices of the scaffold with 85% porosity exhibited more mature collagen fiber (red part) than those with 60% porosity, as shown in Fig. 11(a)-(d). The same results were observed for the sheet-based scaffolds, as shown in Fig. 11(f), (g), (i), and (j). This indicated that the high porosity scaffold had more mature soft tissue in one month of bone repair. Furthermore, comparing the tissue results of the scaffolds with different shapes, it was found that the middle slice of PH60 and the top, middle, and bottom slices of PH85, as shown in Fig. 11(f), (h)-(j), also have more mature collagen fiber than slices at the corresponding positions of PT60 and PT85, as shown in Fig. 11(b), (c)-(e).
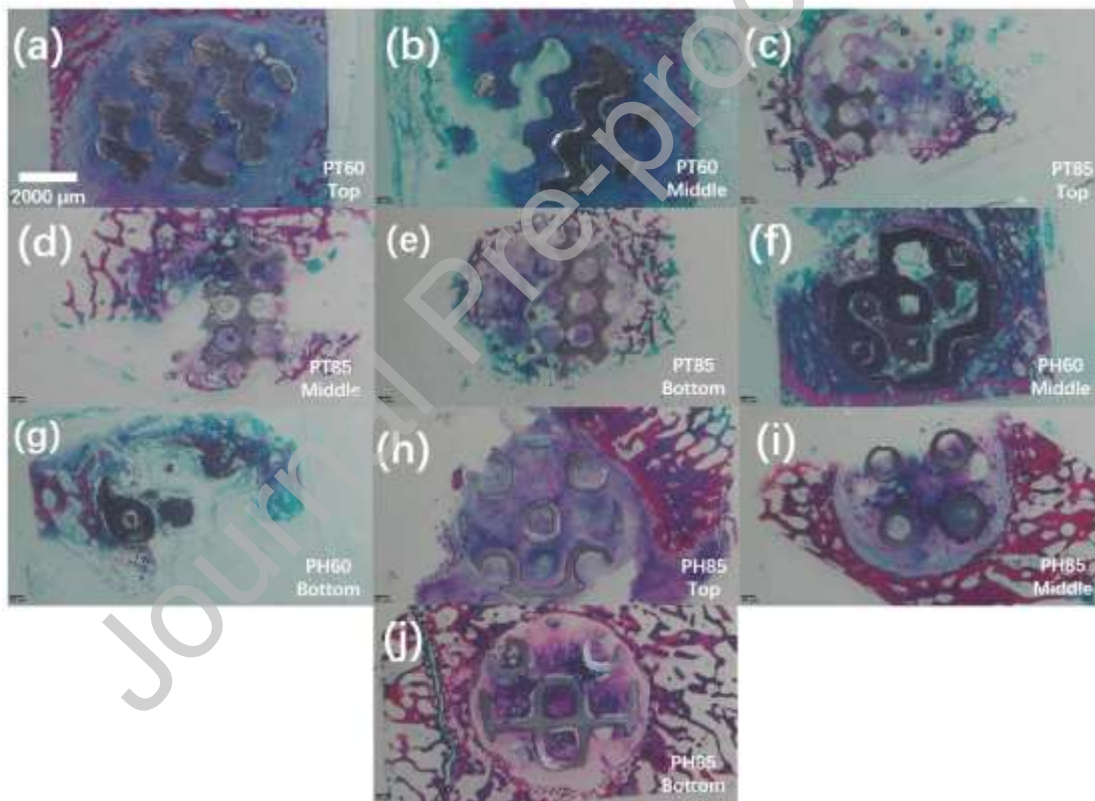

Fig. 11. Results of Masson staining of strut and sheet-based scaffolds with 60% and 85% porosity.

3.3.2 Sirius red staining

Osseous tissue (collagenous fiber) was stained red/purple, while soft tissue was stained yellow in the Sirius red staining process. The red portions inside and outside the scaffold represent newly grown osseous and mature osseous tissue of the host bone, respectively. As shown in Fig. 12(b) to (d), for the bottom slice of the strut-based scaffold with 85% porosity, the osseous tissue grew inwards around the scaffold to a depth of

about 900 μm (360 μm depth for the middle slice). The inward growing osseous tissue can enhance the bond strength of the scaffold and the surrounding tissues of the host bone. However, a small amount of bone tissue was only observed on the right side of the top slice of PT85. The same result was noted in the top and bottom slices of PH60; the red mature tissue connected and crossed the channel of the scaffold in the bottom slice, as shown in Fig. 12(f). The right side of the bottom slice of PH85 was filled by tissue, while hardly any osseous tissue was observed in the top slice. These results indicate that the part that is close to the host bone tissue has a better repair effect. Furthermore, more osseous tissue was found in the top, middle, and bottom slices of the strut-based scaffold with 85% porosity than that in the sheet-based scaffold.

In the one month in vivo experience of pigs, scaffolds with sheet-based structures and a high porosity were conducive to the growth of soft tissue; the strut-based structure and the part closer to the host bone were beneficial to the growth of osseous bone. The Ti6Al4V sheet- and strut-based structures both demonstrated good biocompatibility for bone and have significant application prospects in the clinical bone repair process. In future studies, in vivo experiments with a longer duration may present more noteworthy phenomena.
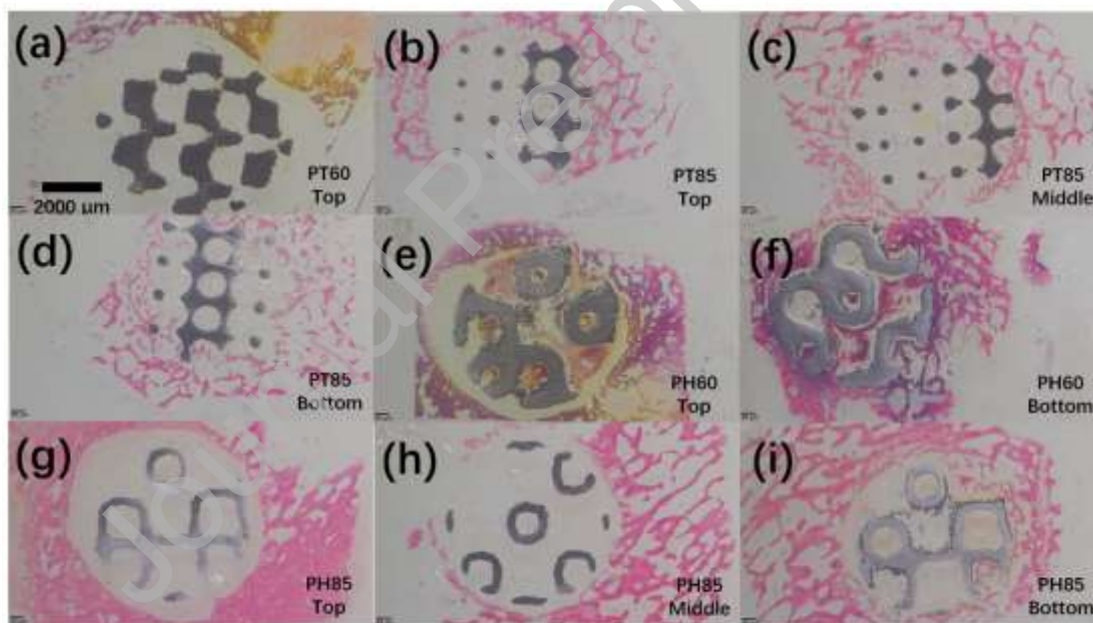
Fig. 12. Sirius red staining of 60% and 85% porosity scaffolds.

4. Conclusions

Strut-based and sheet-based Schwarz-P structures with five different porosities ranging from 60% to 85% were designed and fabricated in this study. To compare the morphology, mechanical properties, and biocompatibility of strut- and sheet-based structures, this study investigated the microtopography, manufacturing error, relative density, roughness, mechanical behavior, and in vivo bone repair behavior of

these two structures at five porosities. These results can provide a deeper understanding of the differences between strut-based and sheet-based TPMS structures. The results can be summarized as follows:

(1) Considering morphology, the as-built porosities were lower than the designed values for both types of structures, and the manufacturing errors of sheet-based structures fluctuated less. The thickness was reduced and cracks were observed in the strut-based samples, while semi-melt powders and the balling phenomenon were observed in sheet-based samples. The relative density of the samples with the lowest porosity was close to that of the block sample. The surfaces of strut-based samples were smoother than those of sheet-based samples.

(2) In terms of mechanical behavior, the elastic modulus, yield strength, first peak stress, and energy absorption of the sheet-based samples were greater than those of the strut-based structures, and the former presented better repeatability. The strut-based structures failed via a layer-by-layer fracturing failure mode; the failure mode of sheet-based structures was a 45° diagonal shear. Both energy absorption and its efficiency for sheet-based structures were greater and more stable than that for strut-based structures. The sheet-based scaffolds exhibited ductile fractures, while the horizonal and vertical struts of strut-based scaffolds demonstrated ductile and brittle fractures, respectively.

(3) The in vivo experiments demonstrated that the sheet- and strut-based scaffolds are good candidates for clinical bone repair owing to the fact that they both exhibit good biocompatibility. The results indicate that the sheet-based structures promote soft tissue growth, while more osseous tissue is found in the strut-based structures. Furthermore, the newly grown bone tissue grew deeper near the host bone, and strengthened the connection between the scaffold and host bone.

In summary, this study investigated the difference between sheet- and strut-based structures in terms of manufacturability, mechanical behavior, and the bone repair effect. The results revealed the manufacturing errors and defects, and the mechanical properties and failure modes of all the structures were compared. This study is significant for guiding suitable decision-making for various purposes. Furthermore, the in vivo test demonstrated the effect of the shape, porosity, and host-bone positioning of the scaffold on the bone repair process, which enhances the understanding of the influence of the scaffold on repair. In future studies, it would be noteworthy to consider a newly designed structure that combines the advantages of these two structures, as well as conducting longer in vivo experiments.

Declaration of Competing Interest

The authors declare that they have no known competing financial interests or personal relationships that could have influenced the work reported in this paper.

CRediT authorship contribution statement

Shuai Ma: Methodology, writing, investigation. **Qian Tang:** Funding, resources. **Changbao Zhu:** Methodology. **Fuyou Wang:** Methodology, resources. **Qixiang Feng:** Validation. **Jun Song:** Methodology. **Rossitza Setchi:** Review & editing, resources. **Chenglong Ma:** Review & editing. **Ran Tao:** Review & editing.

Acknowledgements

Declaration of interests

☒ The authors declare that they have no known competing financial interests or personal

relationships that could have appeared to influence the work reported in this paper.

☐ The authors declare the following financial interests/personal relationships which may be

considered as potential competing interests:

References

[1] Fang Y, Guo Y, Liu T, et al. Advances in 3D bioprinting. Chinese Journal of Mechanical Engineering: Additive Manufacturing Frontiers 2022;1(1): 100011.

[2] Shao H, Nian Z, Jing Z, et al. Additive manufacturing of hydroxyapatite bioceramic scaffolds with projection based 3D printing. Chinese Journal of Mechanical Engineering: Additive Manufacturing Frontiers 2022; 1(2): 100021.

[3] Carluccio D, Xu C, Venezuela J, et al. Additively manufactured iron-manganese for biodegradable porous load-bearing bone scaffold applications. Acta Biomaterialia 2020;103: 346-360.

[4] Arjunan A, Demetriou M, Baroutaji A, et al. Mechanical performance of highly permeable laser melted Ti6Al4V bone scaffolds. Journal of the Mechanical Behavior of Biomedical Materials 2019;102: 103517.

[5] Zhang X, Fang G, Xing L, et al. Effect of porosity variation strategy on the performance of functionally graded Ti-6Al-4V scaffolds for bone tissue engineering. Materials & Design 2018; 157: 523-538.

[6] Kong D, Ni X, Dong C, et al. Bio-functional and anti-corrosive 3D printing 316L stainless steel fabricated by selective laser melting. Materials & Design 2018;152: 88-101.

[7] Ma S, Tang Q, Feng Q, et al. Mechanical behaviours and mass transport properties of bone-mimicking scaffolds consisted of gyroid structures manufactured using selective laser melting. Journal of the Mechanical Behavior of Biomedical Materials 2019;93: 158-169.

[8] Dadbakhsh S, Speirs M, Kruth J, et al. Influence of SLM on shape memory and compression behaviour of NiTi scaffolds. CIRP Annals 2015;64(1): 209-212.

[9] Yang J, Gu D, Lin K, et al. Laser additive manufacturing of bio-inspired metallic structures. Chinese Journal of Mechanical Engineering: Additive Manufacturing Frontiers 2022; 1(1):100013.

[10] Chantarapanich N, Laohaprapanon A, Wisutmethangoon S, et al. Fabrication of three-dimensional honeycomb structure for aeronautical applications using selective laser melting: A preliminary investigation. Rapid Prototyping Journal 2014; 20(6): 551-558.

[11] Feng Q, Tang Q, Liu Y, et al. Quasi-static analysis of mechanical properties of Ti6Al4V lattice structures manufactured using selective laser melting. The International Journal of Advanced Manufacturing Technology 2018; 94(5-8): 2301-2313.

[12] Hollister S J. Porous scaffold design for tissue engineering. Nature Materials 2005;4(7): 518-524.

[13] Fantini M, Curto M, De Crescenzio F. TPMS for interactive modelling of trabecular scaffolds for bone tissue engineering. Advances on Mechanics, Design Engineering and Manufacturing: Proceedings of the International Joint Conference on Mechanics, Design Engineering & Advanced Manufacturing (JCM 2016), 14-16 September, 2016, Catania, Italy, Eynard B, Nigrelli V, Oliveri S M, et al, Cham:Springer, 2017: 425-435.

[14] Barba D, Alabort E, Reed R C. Synthetic bone: Design by additive manufacturing. Acta Biomaterialia 2019;97: 637-656.

[15] Callens S J P, Uyttendaele R J C, Fratila-Apachitei L E, et al. Substrate curvature as a cue to guide spatiotemporal cell and tissue organization. Biomaterials 2020;232: 119739.

[16] Mohammed M I, Gibson I. Design of three-dimensional, triply periodic unit cell scaffold structures for additive manufacturing. Journal of Mechanical Design 2018;140(7): 071701.

[17] Yang E, Leary M, Lozanovski B, et al. Effect of geometry on the mechanical properties of Ti-6Al-4V Gyroid structures fabricated via SLM: A numerical study. Materials & Design 2019;184: 108165.

[18] Al-Ketan O, Rowshan R, Abu Al-Rub R K. Topology-mechanical property relationship of 3D printed strut, skeletal, and sheet based periodic metallic cellular materials. Additive Manufacturing 2018;19: 167-183.

[19] Ambu R, Morabito A. Porous scaffold design based on minimal surfaces: Development and assessment of variable architectures. Symmetry 2018;10(9): 361.

[20] Jung Y, Torquato S. Fluid permeabilities of triply periodic minimal surfaces. Phys Rev E 2005;72(5): 056319.

[21] Ma S, Tang Q, Han X, et al. Manufacturability, mechanical properties, mass-transport properties and biocompatibility of triply periodic minimal surface (TPMS) porous scaffolds fabricated by selective laser melting. Materials & Design 2020;195: 109034.

[22] Bobbert F S L, Lietaert K, Eftekhari A A, et al. Additively manufactured metallic porous biomaterials based on minimal surfaces: A unique combination of topological, mechanical, and mass transport properties. Acta Biomaterialia 2017; 53: 572-584.

[23] Jia H, Lei H, Wang P, et al. An experimental and numerical investigation of compressive response of designed Schwarz Primitive triply periodic minimal surface with non-uniform shell thickness. Extreme Mechanics Letters 2020; 37: 100671.

[24] Yu S, Sun J, Bai J. Investigation of functionally graded TPMS structures fabricated by additive manufacturing. Materials & Design 2019;182: 108021.

[25] Faia-Torres A B, Guimond-Lischer S, Rottmar M, et al. Differential regulation of osteogenic differentiation of stem cells on surface roughness gradients. Biomaterials 2014;35(33): 9023-9032.

[26] Choy S Y, Sun C, Leong K F, et al. Compressive properties of Ti-6Al-4V lattice structures fabricated by selective laser melting: Design, orientation and density. Additive Manufacturing 2017;16: 213-224.

[27] Xu Y, Zhang D, Zhou Y, et al. Study on topology optimization design, manufacturability, and performance evaluation of Ti-6Al-4V porous structures fabricated by selective laser melting (SLM). Materials 2017;10(9): 1048.

[28] Ataee A, Li Y, Brandt M, et al. Ultrahigh-strength titanium gyroid scaffolds manufactured by selective laser melting (SLM) for bone implant applications. Acta Materialia 2018;158: 354-368.

[29] Rho J Y, Ashman R B, Turner C H. Young's modulus of trabecular and cortical bone material: Ultrasonic and microtensile measurements. Journal of Biomechanics 1993;26(2): 111-119.

[30] Arabnejad S, Johnston B, Tanzer M, et al. Fully porous 3D printed titanium femoral stem to reduce stress-shielding following total hip arthroplasty. Journal of Orthopaedic Research 2017;35(8): 1774-1783.

[31] Li D, Liao W, Dai N, et al. Comparison of mechanical properties and energy absorption of sheet-based and strut-based gyroid cellular structures with graded densities. Materials 2019;12(13): 2183.

[32] Soro N, Attar H, Wu X, et al. Investigation of the structure and mechanical properties of additively manufactured Ti-6Al-4V biomedical scaffolds designed with a Schwartz primitive unit-cell. Materials Science and Engineering: A 2019; 745: 195-202.

[33] Arabnejad S, Burnett Johnston R, Pura J A, et al. High-strength porous biomaterials for bone replacement: A strategy to assess the interplay between cell morphology, mechanical properties, bone ingrowth and manufacturing constraints. Acta Biomaterialia 2016;30: 345-356.

[34] Wang D, Yang Y, Liu R, et al. Study on the designing rules and processability of porous structure based on selective laser melting (SLM). Journal of Materials Processing Technology 2013;213(10): 1734-1742.

[35] Wang D, Yang Y, Yi Z, et al. Research on the fabricating quality optimization of the overhanging surface in SLM process. The International Journal of Advanced Manufacturing Technology 2013;65(9-12): 1471-1484.

[36] Mumtaz K, Hopkinson N. Top surface and side roughness of Inconel 625 parts processed using selective laser melting. Rapid Prototyping Journal 2009;15(2): 96-103.

[37] Song J, Tang Q, Feng Q, et al. Effect of remelting process on surface quality and tensile behaviour of a maraging steel manufactured by selective laser melting. In: Scholz S G, Howlett R J, Setchi R (eds). Sustainable Design and Manufacturing 2020. Singapore: Springer, 2021.